rf testbed for thermoacoustic tomography

D. Fallon,[1] L. Yan,[2] G. W. Hanson,[3] and S. K. Patch[4,a)]
[1]*Electronics Research Inc., P.O. Box 1176, Gray, Maine 04039, USA*
[2]*College of Electronics and Information Engineering, Sichuan University, Chengdu 610064, China*
[3]*Department of Electrical Engineering, UW-Milwaukee, Milwaukee, Wisconsin 53211, USA*
[4]*Department of Physics, UW-Milwaukee, Milwaukee, Wisconsin 53211, USA*

(Received 28 October 2008; accepted 22 April 2009; published online 9 June 2009)

Thermoacoustic signal excitation is a function of intrinsic tissue properties and illuminating electric field. De-ionized (DI) water is a preferred acoustic coupling medium for thermoacoustics because acoustic and electromagnetic waves propagate in DI water with very little loss. We have designed a water-filled testbed propagating a controlled electric field with respect to pulse shape, power, and polarization. Directional coupler line sections permit measurement of incident, reflected, and transmitted powers. Both *S*-parameters and E_y measurement show that the electric-field distribution is relatively uniform in testbed. Comparing baseline power measurements to those taken with a test object in place yields power loss in the object, which should correlate to thermoacoustic signal strength. Moreover, power loss—and therefore thermoacoustic computerized tomography signal strength—is sensitive to the orientation of the object to the polarization of the electric field. This testbed will enable quantitative characterization of the thermoacoustic contrast mechanism in *ex vivo* tissue specimens. © *2009 American Institute of Physics.* [DOI: 10.1063/1.3133802]

I. INTRODUCTION AND MOTIVATION

Thermo- and photoacoustics are nonionizing imaging techniques combining the high contrast in electromagnetic (EM) absorption between healthy and cancerous tissues with the high resolution of ultrasound (US). These hybrid systems transmit EM energy and receive outgoing US waves. EM energy is deposited as impulsively in time and as uniformly as possible throughout the imaging object, causing a small amount of thermal expansion. The premise is that cancerous masses preferentially absorb EM energy, heat, and expand more quickly than the neighboring healthy tissue.[1] These masses are internal acoustic sources, creating pressure waves that are detected by US transducers surrounding the object.

Although the photoacoustic effect was discovered a century ago,[2] potential application to medical imaging was not noted until the early 1980s.[3–5] Optical excitation has proven extremely popular for small animal imaging and human applications requiring less than a few centimeters depth penetration.[6–25] Even for imaging with only a few centimeters depth penetration, contrast enhancement is extremely important.[26–33]

A recent survey provides an excellent overview of photoacoustics.[34] For clinical applications requiring greater depth penetration, radio frequency (RF) illumination at 434 MHz has been used, including one clinical trial with approximately 40 volunteers.[35–37] Some reconstructions from these early prototypes were impressive. However, an incomplete understanding of the thermoacoustic contrast mechanism with RF illumination and lack of confidence in the robustness of thermoacoustic imaging have prevented its adoption into widespread clinical use.

We therefore have developed a testbed that illuminates with a tightly controlled electric field. Sketches comparing the University of Wisconsin-Milwaukee (UWM) testbed to other TCT systems[38–41] are shown in Fig. 1. Unlike thermoacoustic imaging systems built to date, the UWM testbed has the following features:

(1) Relatively low illumination frequency of 108 MHz. This ensures good depth penetration compared to microwave and photoacoustic systems.
(2) A DI water bath, rather than oil. DI water provides excellent acoustic coupling with minimal US and EM loss of 108 MHz.
(3) Aluminum walls (rather than glass or plexi) which are RF tight.
(4) An aluminum lid with good contact fingers (rather than air/water interface) which is also RF tight.
(5) A transducer shield, eliminating RF interference from RF illumination pulse.
(6) Well-matched input and output probes that efficiently transmit power through the testbed. A well-matched input probe minimizes power reflected back to the amplifier. A well-matched output probe efficiently transmits power out of the testbed. This minimizes standing waves, keeps the testbed Q low, and preserves the short input pulse shape.
(7) A clear analytical model of the E-field in the vicinity of the test object. The E-field is primarily a TE10 wave with a very small component of TE103 standing wave.
(8) Directional coupler line sections permit measurement in incident, reflected, and transmitted powers. Comparing the baseline power measurements to those taken with a test object in place, we can estimate power loss in the object and correlate to TCT signal strength.

[a)]URL: http://www.uwm.edu/patchs.

 © 2009 American Institute of Physics

Author complimentary copy. Redistribution subject to AIP license or copyright, see http://rsi.aip.org/rsi/copyright.jsp

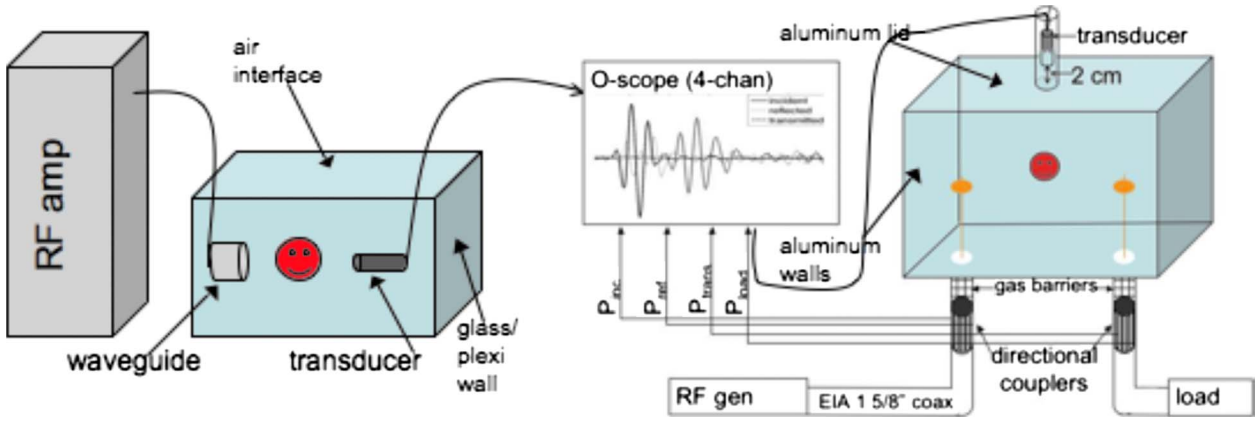

FIG. 1. (Color online) *l* denotes the common TCT system setup and *r* denotes the sketch of the UWM testbed.

This last point is important because the rate of loss cannot be too high, lest the patient's tissue be damaged by excessive heating. Indeed, the Specific Absorption Rate (SAR) is limited by the U.S. Food and Drug Administration to no more than 12 W/kg. ANSOFT HFSS models used to design the testbed indicate that 1W input power can generate over 3 W/kg SAR in small test objects of interest located at the central *E*-field max. Currently, photo- and thermoacoustic systems are starved for signal to noise (S/N) and signal averaging is typically required to reduce noise to acceptable levels. The testbed will allow us to directly correlate SAR levels to signal strength. Current SAR safety limits assume pulse durations of several hundred microseconds in magnetic resonance imaging (MRI) and nearly continous wave (CW) illumination for cell phones. Our pulse widths are shorter than 1 μs so the testbed will prove an important tool for determining acceptable instantaneous SAR levels for such short duration pulses. Furthermore, the testbed will permit us to quantify the effect of potential contrast agents that may improve S/N.

This article begins with a brief review of the physical model upon which thermoacoustic imaging is premised (Sec. I A). From this model we then outline system specifications (Sec. I B). Methods and materials are described in Secs. II and III, respectively. Finally, we conclude with results validating the performance of the testbed in Sec. IV.

A. Thermoacoustic model

Thermoacoustic image reconstruction is an inverse acoustic source problem. Frequently the source term is assumed to be quasistatic and the governing equation is written as

$$\frac{\partial^2 p}{\partial t^2}(\mathbf{x},t) - \Delta p(\mathbf{x},t) = \frac{\partial I(t)}{\partial t} S(\mathbf{x}), \tag{1}$$

with zero initial conditions. *S* represents conversion of EM energy into heat which subsequently causes thermal expansion and increased pressure *p*. *I* is the pulse envelope and we have normalized the speed of sound to be one. Typically, *I* is made as impulsive as possible so that $I \sim \delta$, the Dirac-δ function. Thermoacoustic image reconstruction is based on the solution of the wave [Eq. (1)], which can be written in terms of spherical means.[42] Thermoacoustic reconstruction of the unknown function $S(\mathbf{x})$ is appealing to mathematicians as a (relatively) stable inverse acoustic source problem, which is equivalent to inverting the spherical Radon transform—and therefore similar to x-ray computerized tomography. A plethora of reconstruction methods for ideal thermoacoustic computerized tomography (TCT) data exist in both two and three dimensions.[43–47] These reconstruction techniques require measurement of pressures on a surface completely surrounding the reconstruction region. In clinical practice, measurements may be limited to a relatively small solid angle. Reconstruction of limited angle data is highly unstable outside of the "audible zone"[48] but recent results demonstrate good image quality from both iterative[7,49–51] and direct[52,53] reconstruction methods.

Because thermoacoustics is an inverse source problem, thermoacoustic pulses are *outgoing* only and therefore travel only half as far as the standard US pulses. Acoustic pulses attenuate exponentially with distance traveled[54] so thermoacoustics can potentially provide up to twice the depth penetration of US if the heating EM pulse penetrates deeply.

Breast imaging with RF excitation at 434 MHz (Refs. 36–38) has produced some compelling images. Nevertheless, TCT has not progressed into clinical use. To determine whether TCT contrast can be robust and also clinically relevant, we rewrite Eq. (1) including all basic physical parameters rather than lumping them into *S*,

$$\frac{\partial^2 p}{\partial t^2}(\mathbf{x},t) - \Delta p(\mathbf{x},t) = \left(\frac{\beta B}{C}\right)(\mathbf{x})\sigma(\mathbf{x};\omega)\frac{\partial |\mathbf{E}(\mathbf{x},t)|^2}{\partial t}, \tag{2}$$

where β, *C*, and *B* represent thermal expansion coefficient, specific heat, and bulk modulus, respectively. $\sigma(\mathbf{x},\omega)$ represents electrical conductivity, (with ω included as a reminder that dispersion is significant). **E** is the electric field within the object which is a strong function of the dielectric constant as well as conductivity and applied field. Note that the source terms β, B, C, σ are intrinsic tissue properties that should be nearly constant over time. **E**, however, is a function of intrinsic tissue dielectric properties and applied electric field. Penetration of the applied electric field into the object of interest is highly dependent upon boundary conditions and polarization of **E**. Therefore, polarization of the applied field is critical. Robust TCT imaging may therefore require mul-

Author complimentary copy. Redistribution subject to AIP license or copyright, see http://rsi.aip.org/rsi/copyright.jsp

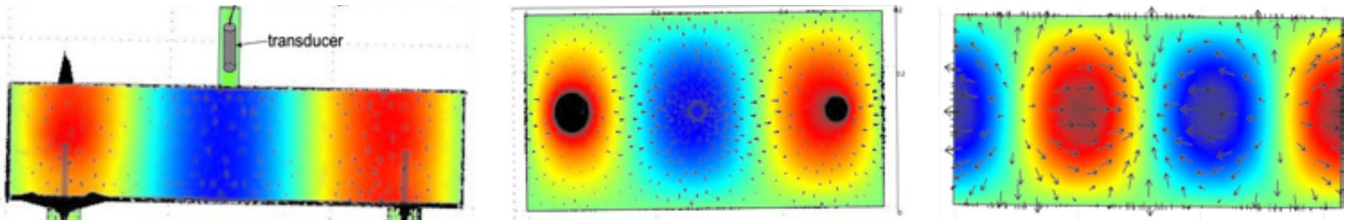

FIG. 2. (Color online) COMSOL simulations of $\mathbf{E}_z$, with arrows indicating surface electrical current. Left and center: testbed cavity modes have strong standing waves with maxima at the input and output probes; right: one snapshot of traveling waves moving along the waveguide/transmission line.

tiple data acquisitions corresponding to the illuminating electric fields with different polarizations. (We envision 3 acquisitions corresponding to three mutually orthogonal polarizations.)

Intrinsic tissue properties may limit the efficacy of thermoacoustics. Bulk modulus is considered to be relatively constant within soft tissues but is also known to be a function of temperature. Thermal conductivity and specific heat have also been reported to exhibit 50% variation between fat as opposed to muscle and organ tissues.[55] Good EM contrast has been reported in the RF range.[1,56] In particular, over the 10–100 MHz range contrast is significant.[57] However, recent dielectric studies on excised breast tissue give a sobering perspective on microwave heating for thermoacoustic breast imaging. Over the 500 MHz–20 GHz range, adipose tissue has a high EM contrast to nonadipose tissue and malignant tissue is virtually indistinguishable from nonadipose healthy tissue.[58,59] RF waves penetrate far better than microwaves, so we designed our testbed to enable studies of TCT contrast under a controlled electric field with a carrier frequency near 100 MHz.

B. Thermoacoustic system specifications

From the formulation in Eq. (2) it is clear that strong pressures are generated when the source term is large, requiring that $[\partial|\mathbf{E}(\mathbf{x},t)|^2]/\partial t$ be large. Pressures are generated only for $(\mathbf{x},t)$ at which the *E*-field has a large amplitude and also a large temporal derivative. Therefore, a short and high-power EM pulses must be applied. Illumination frequencies corresponding to short wavelengths in tissue create spatially nonuniform heating, with cold spots separated from hot spots by a quarter wavelength. Wavelengths in soft tissue decreased from approximately 7 cm at 500 MHz down to just a few millimeters at 20 GHz so *uniform* excitation is difficult to achieve over a large imaging volume. Nevertheless exciting small animal studies (for instance, with Rhesus monkeys) have been documented in.[60,61] We work with a carrier frequency near 100 MHz, so that in soft tissue $\lambda > 32$ cm, ensuring reasonably strong heating over an imaging field of view of at least 8 cm $< \lambda/4$. This is consistent with state of the art magnetic resonance imaging. 3 T MRI scanners excite by transmitting 128 MHz RF pulses which have 30 cm wavelengths in the tissue. At 128 MHz RF deposition is far less uniform than at 64 MHz but well within correctable limits.[62] Boundary conditions for the electric field require continuity of $\mathbf{E} \times \mathbf{n}$. It is therefore critical that we control for polarization of the electric field relative to the objects of interest. Finally, clean TCT pressure measurements ought not be corrupted by the electrical interference from the illuminating pulse.

II. METHODS

The ideal illuminating pulse would be uniform in space and impulsive in time. The next best situation would be to create a traveling wave that would generate an electric field which decays smoothly in space and could be easily pulsed with respect to time. Terminated waveguide components can be purchased off the shelf for EM propagation in air. In order to maintain good acoustic coupling, however, we propagate in DI water, which has very low acoustic and EM absorptions. Water-filled TEM cells to generate uniform **E** fields have been reported.[63] To maintain a tight RF environment, we modify the classical TE103 cavity to include the properties of a transmission line.

The testbed is a hybrid between a rectangular cavity supporting the TE103 mode and a rectangular waveguide carrying the dominant TE10 mode. The rectangular testbed forms a cavity but with identical input and output probes positioned at the first and third *E*-field local maxima, as depicted in Fig. 2. These symmetric probes exploit reciprocity, efficiently coupling into the TE10 mode which propagates across the testbed and out to a dummy load. A lossless TE103 resonant cavity would maintain strong standing waves long after excitation. Our testbed, however, is closer to a waveguide that efficiently propagates traveling waves to the dummy load so the temporal envelope of the *E*-field inside the testbed mimics that of the input pulse. The small amount of power reflected inside the testbed creates standing waves with local maxima at the input and output probes, as depicted in Fig. 2, but most of the power travels from the input probe through the output probe to the dummy load. Testbed design was done in the frequency domain using commercial finite element numerical solvers. Preliminary design was done in COMSOL but final testbed design was completed using ANSOFT HFSS.

To efficiently propagate from air-filled coaxial line into the water-filled testbed, a gas barrier was custom designed at the Electronics Research Inc. (ERI) to provide a good match. The gas barriers gradually transition from air-filled 1 5/8 in. coaxial line to the water-filled testbed, as depicted in Fig. 3. The water-filled cavity is fed from below by an air-filled coaxial line (1 5/8 in. EIA). The design criteria are twofold; first the water must be kept in the cavity and out of the line, second there must be a good RF match between the line and the cavity for the efficient transfer of power from the transmitter to the test-bed and from the test-bed to the load. The

Author complimentary copy. Redistribution subject to AIP license or copyright, see http://rsi.aip.org/rsi/copyright.jsp

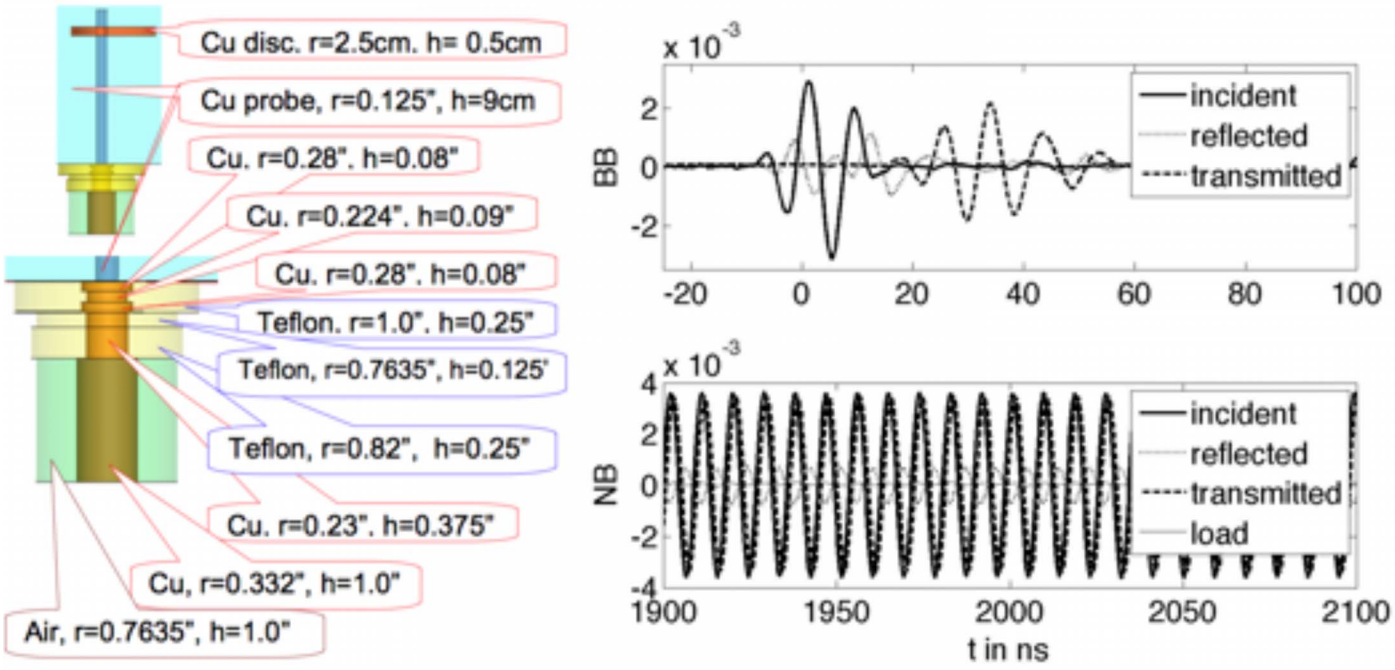

FIG. 3. (Color online) Left: Adjustable copper disks and custom gas barrier. Right: BB and few cycles from a NB pulse.

first criteria is met by incorporating a coaxial gas barrier which consists of a dielectric insulator and silicon rubber gaskets. The insulator is a sudden discontinuity in the line which must be compensated for by a step in the inner conductor diameter. The design is straightforward, using the techniques in Ref. 64. The second criterion is met by realizing that the cavity is simply a water filled waveguide. A coaxial to waveguide adaptor is designed using the techniques in Ref. 65. The adaptor is a probe type consisting of an extension of the coaxial lines, inner conductor, and a larger diameter disk. The spacing of the probe from the end wall of the waveguide and the height of the disk control the quality and bandwidth of the match. Adjustable copper disks in the finalized testbed are used to optimize the field patterns.[66–68]

Compare plots in Fig. 3 of the incident, reflected, and transmitted powers of pulses with a center frequency of 110 MHz. The broadband (BB) pulse duration is approximately two cycles (20 ns), whereas the narrowband (NB) pulse duration is approximately 400 cycles (4 μs). Although the BB pulses are significantly distorted by the testbed, they die out relatively quickly. NB pulses with carrier frequency within the testbed's transmission window are very well preserved. Results on the transmission efficiency of the testbed is discussed in Sec. IV. The 24 ns time delay corresponding to the travel time between directional coupler line sections is readily apparent in the plots of BB pulses and can also be seen in the NB plots by taking the 10 ns cycle time into account.

S-parameters were measured at the ERI using a network analyzer. At the UWM, *s*-parameters (shown in Fig. 4) were manually computed from the incident and reflected waveforms measured using directional coupler line sections. The estimates from NB pulses of 4 μs duration driven with carrier frequencies at 1 MHz intervals over the range 70–130 MHz were computed simply by comparing L^2 norms of the incident, reflected, and transmitted pulses.

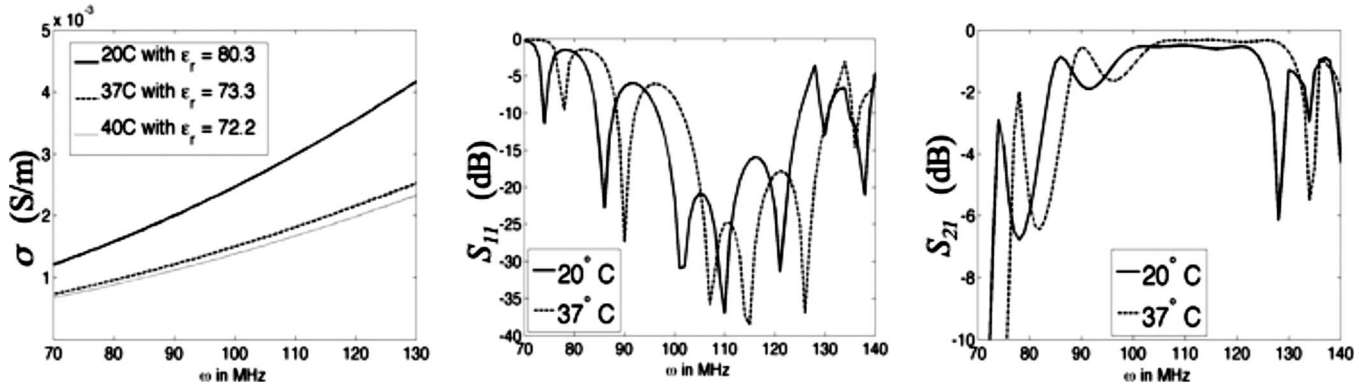

FIG. 4. Modeled temperature and frequency dependence of dielectric properties of water and transmission properties of the testbed. Left: $\sigma=\sigma(\omega,T)$; whereas $\epsilon_r'=\epsilon_r'(T)$. Center and right: S_{11} and S_{21} at room and body temperatures, respectively.

Author complimentary copy. Redistribution subject to AIP license or copyright, see http://rsi.aip.org/rsi/copyright.jsp

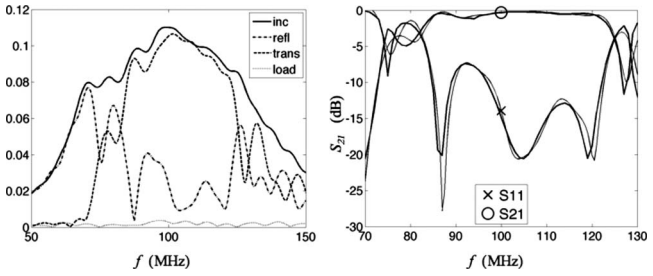

FIG. 5. Left: Spectra of BB directional coupler data. "Load" refers to the reflection off of the dummy load. Right: estimates of *s*-parameters, NB in thick line, and BB in thin line.

$$S_{11}(k) = 10\log_{10}(P_{\text{refl}}/P_{\text{inc}}) = 20\log_{10}(\|V_{\text{refl}}\|_{L^2}/\|V_{\text{inc}}\|_{L^2}),$$

$$S_{21}(k) = 10\log_{10}(P_{\text{trans}}/P_{\text{inc}}) = 20\log_{10}(\|V_{\text{trans}}\|_{L^2}/\|V_{\text{inc}}\|_{L^2}). \quad (3)$$

The estimates from the spectral content of BB pulses of 20 ns duration were computed as follows:

$$S_{11}(k) = 20\log_{10}[|\mathbf{F}V_{\text{refl}}(k)|/|\mathbf{F}V_{\text{inc}}(k)|],$$

$$S_{21}(k) = 20\log_{10}[|\mathbf{F}V_{\text{trans}}(k)|/|\mathbf{F}V_{\text{inc}}(k)|]. \quad (4)$$

The BB estimates were reasonable but less consistent than the NB estimates, as shown in Fig. 5.

The *E*-field was measured using a slotted top and monopole antenna fabricated in the UWM instrument shop. A "chimney" located directly above the central *E*-field maximum of standing modes shields a single-element US transducer from the RF interference. As seen in Fig. 6, the testbed sides protrude above the interior water level. This permits overfilling so that the waterline inside the chimney can be easily maintained at least 1 cm higher than inside the testbed, providing significant shielding from RF interference (RFI), as shown in Fig. 6. The objects of interest are placed directly below the transducer chimney with positioners designed to maintain the electric field.

III. MATERIALS

The testbed was manufactured at ERI. Interior testbed dimensions are $24\times15\times64$ cm^3. Walls and top are 1/4 in. aluminum. Silver contact fingers (Orbel #0097013911) maintain good electrical contact between the top and the sides. When the top is in position, the testbed sides protrude 1/4 in. above the upper surface of the top, permitting slight overfilling of the testbed, as depicted in Fig. 6. This ensures that the water bath always completely fills the interior of the testbed and that the water level in the chimney can easily be kept 10 mm above the testbed interior. The chimney dimensions are 25 mm-ID, 34 mm-OD, and 102 mm in height above the water level *inside* the testbed.

The EIA 1 5/8 in. coaxial copper line and connectors (MYATT) transmit power into the testbed and from the testbed to load. 50 Ω connections were used throughout, for both rigid and flexible coaxial lines. For the testbed validation, low power pulses were transmitted from a signal generator (Rohde & Schwarz, SML01) and signals were recorded on a four-channel oscilloscope with 1 GHz bandwidth (Tektronix DPO7104). During most measurements the oscilloscope's bandwidth was set to 200 MHz. Two directional coupler line sections (Bird #4715–000) fitted with 50 dB attenuating elements having BNC connections (Bird #4274–000) were used to monitor incident and reflected power into the testbed as well as power transmitted through the testbed and reflected off of the load, as depicted in Fig. 3. To accurately assess *s*-parameters and pulse propagation times, a set of new RGI-174 cables of identical length (4 ft) carry a signal from the directional coupler elements to the oscilloscope. *S*-parameter estimates from the directional coupler measurements are compared to those taken at ERI with a network analyzer (HP #8753E) and also to numerical models in Sec. IV.

The slotted top and monopole antenna used to measure the *E*-field were fabricated in the UWM instrument shop. The top was made of 1/2 in. aluminum with a 3/8 in. slot running along the center line. The 3/8 in. slot was cut only 3/8 in. deep to hold the copper disk in place. A much thinner ($\sim$1/16 in.) slot cut through the bottom of the slotted top allowed the inner conductor of a monopole antenna to protrude into the DI water below. The top was marked at 1 cm intervals to facilitate mapping of the electric field along the axis of propagation. A monopole antenna with a copper disk of radius 1.23 in. provided the ground. The outer braid of a RG188 coaxial cable was pulled back so that the center conductor and plastic insulator could be inserted through a 1/16 in. hole in the center of the copper disk. The outer braid was then soldered to the top of the copper disk. Initially, the monopole protruded over 9 cm through the disk. Multiple mappings of the *E*-field with respect to the distance from the

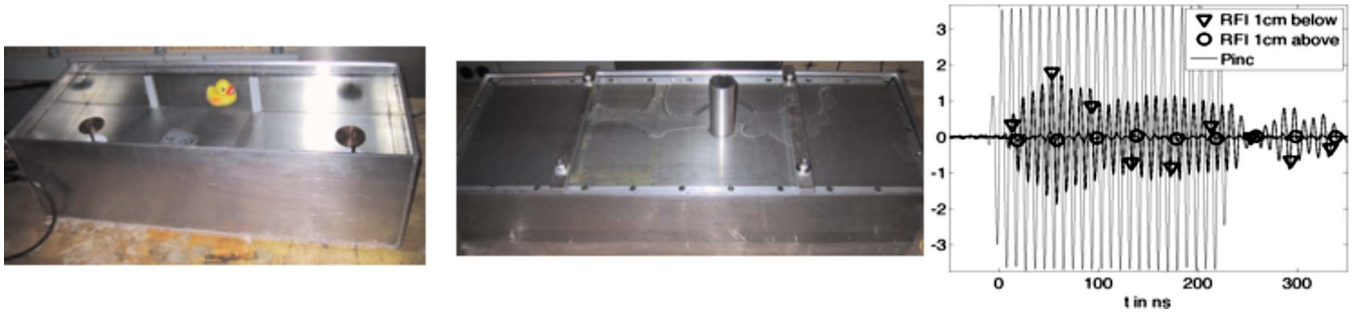

FIG. 6. (Color online) Left: Interior of testbed. Center: Water level is slightly higher than the testbed top. Right: The RFI experienced by the transducer at different elevations in the chimney.

Author complimentary copy. Redistribution subject to AIP license or copyright, see http://rsi.aip.org/rsi/copyright.jsp

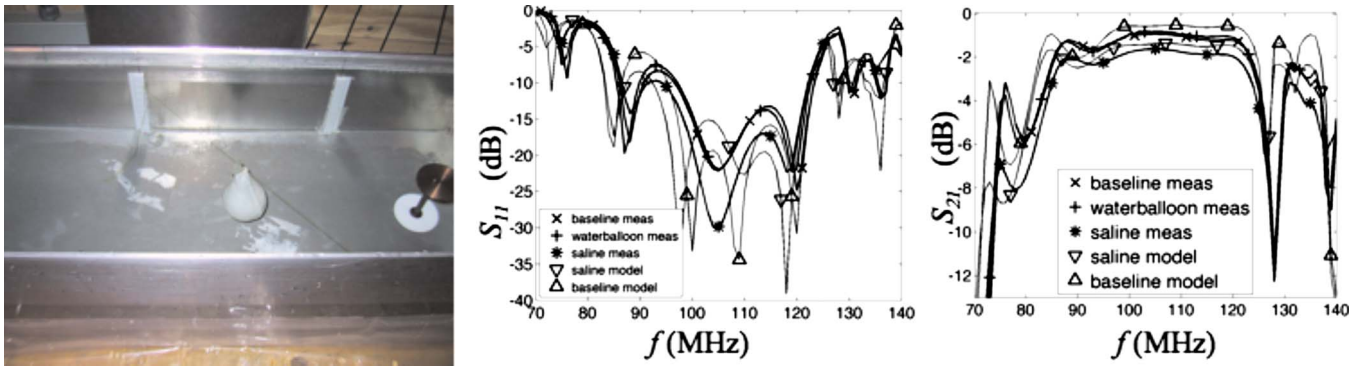

FIG. 7. (Color online) *S*-parameters for an empty testbed, water- and saline-filled balloons. Left: Saline-filled balloon held in position by the embroidery floss. Center and right: s_{11} and s_{21}, respectively.

input power port were made with this antenna. After each measurement, approximately 5 mm of the center conductor was snipped off, leaving a shorter antenna.

Two different electromagnetically lossy phantoms were placed below the transducer chimney to quantify power loss, which corresponds to heating and ultimately TCT signal. A balloon and a large syringe filled with approximately 75 ml of 0.9% physiologic saline (Baxter) caused a significant transmission loss. The syringe caused significant loss only when it was aligned with the *E*-field. To minimize perturbation of the *E*-field, phantoms were positioned using embroidery floss. Thin white fiberglass reinforced plastic (Royal Moldings) was cut with multiple slits at 1 cm intervals and was secured with a rubber cement to the testbed interior, as seen in Fig. 6. A thread is attached to the testbed sides at the slits. The saline-filled balloon and syringe were secured, as shown in Figs. 7 and 8. The water-filled balloon was more buoyant than the saline-filled balloon so it was positioned similarly but upside-down.

IV. RESULTS

Several methods have been used to validate the testbed design including RFI shielding efficacy, EM propagation efficiency as measured by *s*-parameters, *E*-field fidelity as measured by a monopole slot antenna, and power loss due to lossy inclusions in the testbed.

A. RFI shielding

The efficacy of shielding the transducers from RFI inside the chimney was validated at various transducer heights above and below the interior water level. 13 dBm pulses of 240 ns duration were propagated into the testbed containing only DI water, so we expect no detectable acoustic signal to be generated at such low power levels. Incident and transmitted waveforms recorded by the directional coupler are compared to RFI signal picked up by the transducer in Fig. 6. Elevating the single element transducer 1 cm above the interior waterline reduces the RFI dramatically.

B. Transmission efficiency

Dielectric properties of water are strongly dependent upon temperature, as depicted in Fig. 4. Conductivity σ shows dispersion and temperature dependence over the frequency range 70–130 MHz, whereas the dielectric constant ϵ_r shows primarily only temperature dependence over this frequency range. These parameters are used to model *s*-parameters for the testbed as a function of the temperature. The temperature therefore strongly affects the resonant frequency and transmission efficiency of the testbed. S_{11} and S_{21} were modeled assuming perfectly conducting testbed walls.

S-parameters measuring the efficiency with which pulses propagate through the testbed were measured at the ERI using a network analyzer and at UWM using directional couplers. Results agree well above −10 dB but with the direc-

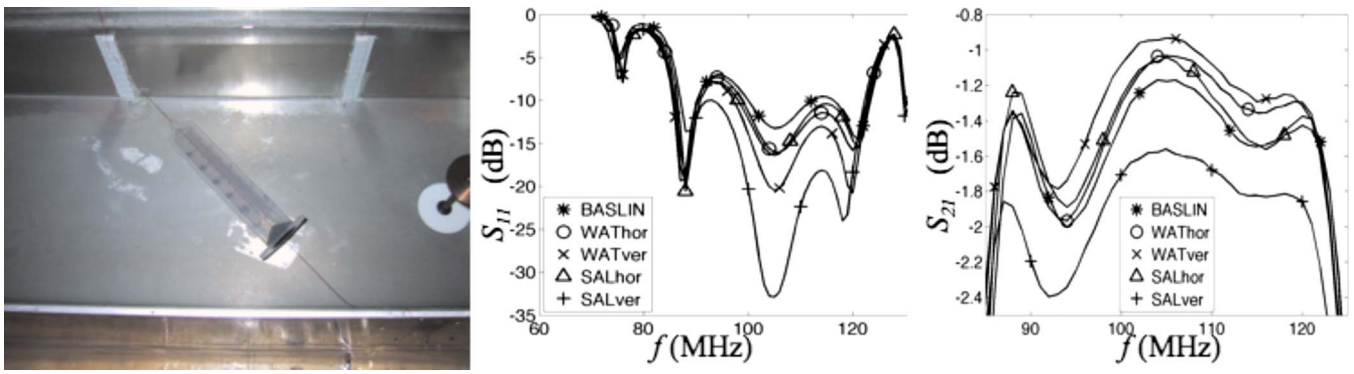

FIG. 8. (Color online) *S*-parameters for an empty testbed, water- and saline-filled syringes. Left: Syringe mounted horizontally. Center and right: s_{11} and s_{21}, respectively.

Author complimentary copy. Redistribution subject to AIP license or copyright, see http://rsi.aip.org/rsi/copyright.jsp

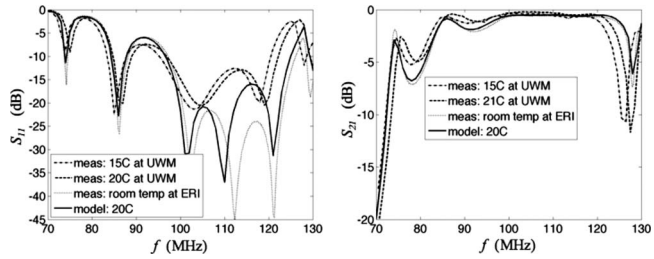

FIG. 9. *S*-parameters measured with a network analyzer at the ERI and estimates from NB directional coupler data measured at the UWM compare well to those computed using the dielectric constants in Fig. 4.

tional coupler readings of low power pulses we are not yet able to recover $S11<-20$ dB at the UWM. Nevertheless, over the frequency range 98–121 MHz $S_{11}<-10$ dB and $S_{21}>-1$ dB in both directional coupler measurements at the UWM at 21 °C, room temperature measurements at the ERI, and also in simulations assuming 20 °C, as depicted in Fig. 9. This broadband response ensures that the temporal envelope of the *E*-field inside the testbed mimics that of the input power rather than resonating inside the aluminum cavity.

The *S*-parameters estimated from the measurements of a single BB pulse compare reasonably well to those estimated from many NB data sets corresponding to the different center frequencies throughout the range of interest. 61 data sets were collected with carrier frequencies at 1 MHz intervals over the frequency range 70–130 MHz to generate the NB plots in Fig. 5. The BB estimates agree with the NB estimates very well above −10 dB, when the signal strength is high. The *S*-parameter estimates computed from the directional coupler measurements of incident, reflected and transmitted powers may not be as quantitative as those from calibrated network analyzer data. To validate the estimates from the UWM directional couplers we compared the measurements from different element orientations and combinations. Each of the four directional coupler ports were labeled with a number and default direction #1 ~ ↑ ~ incident, #2 ~ ↓ ~ reflected, #3 ~ ↓ ~ transmitted, and #4 ~ ↑ ~ reflection off of load. "SOP" refers to the elements oriented according to the labels on their ports; "rev" refers to the elements oriented opposite to the labels. The elements were also labeled 1, 2, 3, and 4. Eight data sets were collected starting with the elements in their corresponding ports in the SOP orientation. The NB and BB data were collected and then the element orientations were reversed and the data were recollected. The elements were then reordered, shifting elements 1, 2, 3, and 4 into ports 2, 3, 4, and 1, respectively. The element orientation was first set to SOP before both NB and BB data were collected. The element orientation was reversed to the rev orientation before the NB and BB data were recollected. This process continued, shifting elements 1, 2, 3, and 4 into ports 3, 4, 1, and 2. Finally, elements 1, 2, 3, and 4 were rotated into ports 4, 1, 2, and 3. *S*-parameters estimated from these permutations of elements and their orientations were consistent to about 1/2 dB, as shown in Fig. 10.

C. E_y measurements

The monopole antenna and slotted top were used to get rough estimates of the *E*-field as a function of *z* position along the center $x=a/2=12$ cm line. Narrowband pulses of 4 μs duration at a carrier frequency 105 MHz were used throughout. Peak-to-peak voltage values at each *z* location were taken as proportional to the $E_y(z)$. The data were collected first with the monopole protruding approximately 9.5 cm below the slotted top. The antenna was positioned between the input and output power probes at 1 cm intervals. After collecting a sweep along the *z* centerline, approximately 0.5 cm was snipped off the antenna and the data were recollected. This process was repeated until only 1 cm was left of the antenna. The water temperature rose somewhat during this process which started at 22 °C and ended at 23 °C.

The results corroborate the *s*-parameters, in that the testbed behaves primarily as a transmission line. Peak-to-peak values for the 9.5 cm antenna are plotted in Fig. 11 (left) and referred to as $E_{\text{meas}}(z)$. Because the testbed is not a perfect transmission line, a small amount of TE103 is superimposed on the large TE10 component. The slight decay of TE10 is modeled by taking account of the loss in the DI water but ignoring the loss in the aluminum walls. We expect the TE10 component to decay like $e^{-\alpha z}$ where $\gamma=\alpha+j\beta$ and

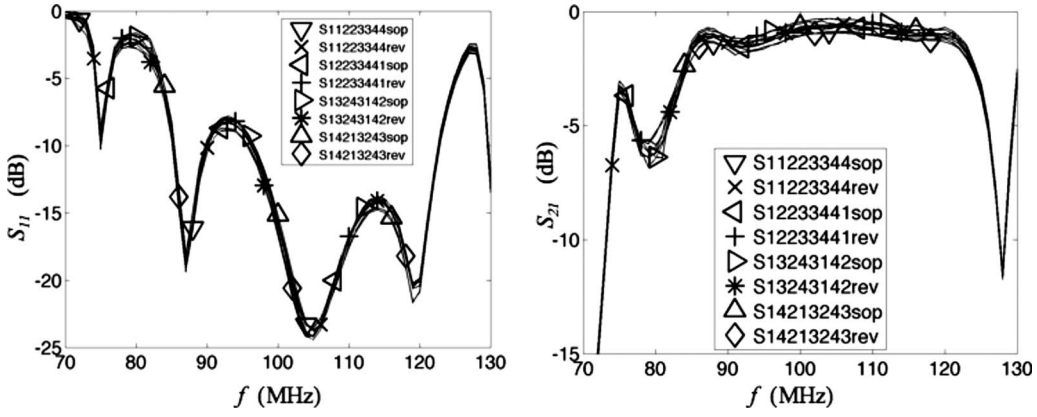

FIG. 10. *S*-parameter estimates from various element combinations and orientations. Left: S_{11}. Right: S_{21}.

Author complimentary copy. Redistribution subject to AIP license or copyright, see http://rsi.aip.org/rsi/copyright.jsp

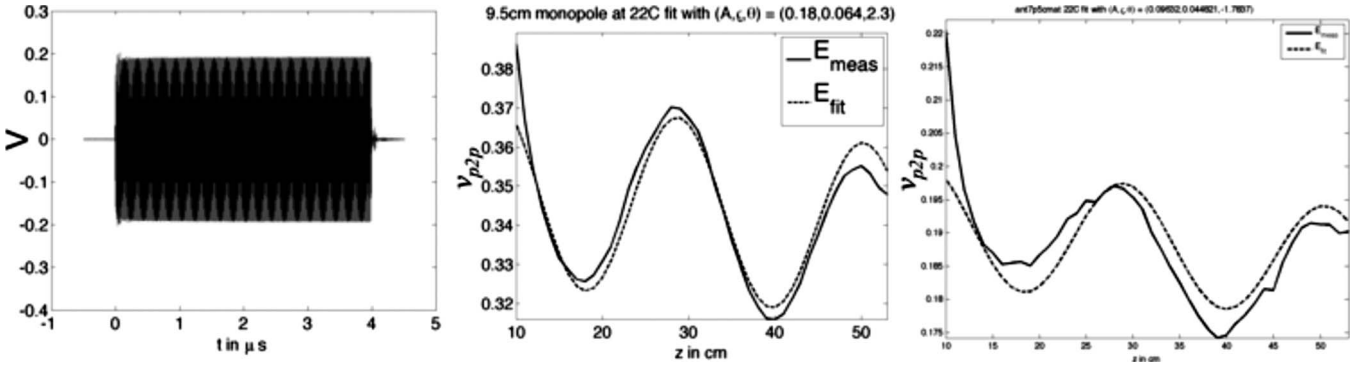

FIG. 11. *E*-field measurements with 9.5 cm monopole antenna. Left: Peak-to-peak values of raw voltage measurements provide *A*. Center: Modeled data compares well to measurements for 9.5 cm monopole. Right: Model and measurement agree poorly for 7.5 cm monopole.

$$\gamma^2 = k_c^2 - k_o^2\epsilon_r(T) = k_c^2 - k_o^2\left(\epsilon_r'(T) - j\frac{\sigma}{\omega\epsilon_o}\right)$$

$$= (0.0729 + j14.6)^2, \tag{5}$$

where we have used dielectric values at 22 °C. We model reflection at the output end of the testbed with $\rho e^{i\theta}$, where $\rho, \theta \in \mathbb{R}$. Then for each antenna z location the time series recorded on the oscilloscope are modeled as

$$v(z,t) = A\mathcal{R}e([e^{-\gamma z} + \rho e^{i\theta}e^{-\gamma(2L-z)}]e^{i\omega_o t}), \tag{6}$$

$$= A\mathcal{R}e([1 + \rho e^{i\theta}e^{-\gamma 2(L-z)}]e^{-\gamma z}e^{i\omega_o t}), \tag{7}$$

$$= Ae^{-\alpha z}\mathcal{R}e([1 + \rho e^{i\theta}e^{-2\gamma(L-z)}]e^{i(-\beta z+\omega_o t)}), \tag{8}$$

where $L=0.64$ is the length of the testbed in meters and $\omega_o = 2\pi$ 105 MHz is the carrier frequency. As shown in Fig. 11 (left), the peak-to-peak values of the measured waveforms are clearly defined. Each 4 μs pulse contains about 400 cycles and suffer slight waveform distortions at the beginning and end of each pulse. Only the middle 200 cycles were used to estimate peak-to-peak values plotted in Fig. 11 (right). Multiplying by $e^{\alpha z}$ yields

$$v_{p2p}(z)e^{\alpha z} = 2A\mathcal{R}e([1 + \rho e^{i\theta}e^{-2\gamma(L-z)}]), \tag{9}$$

$$= 2A\mathcal{R}e(1 + \rho e^{-\alpha 2(L-z)}e^{i[\theta-2\beta(L-z)]}), \tag{10}$$

$$= 2A\{1 + \rho/2e^{-\alpha 2(L-z)}[e^{i[\theta-2\beta(L-z)]} + e^{-i[\theta-2\beta(L-z)]}]\}, \tag{11}$$

$$= 2A + e^{-2\gamma(L-z)}(A\rho e^{i\theta}) + e^{-2\gamma^*(L-z)}(A\rho e^{-i\theta}), \tag{12}$$

where γ^* denotes the complex conjugate of γ. A linear least-squares fit recovers 2A, $A\rho e^{i\theta}$ and $A\rho e^{-i\theta}$ from which the desired parameters, A, ρ, and θ are recovered. Substituting back into Eq. (9) to recover v_{p2p} yields reasonable results, shown for the 9.5 cm monopole in Fig. 11 (center). The agreement was not as good for shorter monopole antennae partly because the quality of the measured data E_{meas} degrades as the antenna becomes shorter. However, we consistently underestimate the decay, as seen in Fig. 11 (right).

D. Lossy objects and transmitted power

To confirm that highly conductive objects indeed result in a transmitted power loss when placed in the testbed, we illuminated balloons filled with approximately 75 ml of fluid. The NB pulses of 4 μs duration illuminated the objects at a center frequency of 110 MHz. The sampling rate was set extremely high at 5 GHz to ensure accurate power estimates from the L^2 norms of the signals.

The presence of a water balloon filled with approximately 75 ml of water changes the percentages of reflected and transmitted powers only slightly. The balloons were filled and left overnight nearby the testbed to ensure they were in thermal equilibrium. The baseline data were collected with the testbed filled only with room-temperature water. The presence of the water balloon had a minor impact on the transmitted power. Presumably this is because the thin walls of the balloon have a different dielectric constant than 23 °C water. The balloon filled with saline solution, however, *decreased* both the reflected and transmitted powers. The transmitted power decreased by about 1 dB over the range 85–120 MHz, indicating that the saline solution absorbed more power than the water-filled tank and water balloon. The reflected power decreased even more, presumably because the saline solution acted as a power sink.

As depicted in Fig. 8 center and right, both reflected and transmitted powers dropped significantly when a 60 ml saline-filled syringe was oriented vertically in the testbed. This indicates that the vertical syringe absorbed significant power, reducing even the reflected power. *s*-parameters from the baseline, water-only, and horizontally aligned syringe appear to be consistent. The only difference between the baseline and water–filled syringe is the presence of the plastic syringe and rubber cap. Because these measurements were done at a low input power (13 dBm) variations between the other realizations may not have physical significance.

ACKNOWLEDGMENTS

Thanks to Mike Schrauth and Andrew Eckhart for making the positioners and collecting *s*-parameter data. Thanks to WUWM for loaning the directional coupler line sections. Thanks to Tom May for the advice on installation—and hard work implementing it. Thanks to Jerry Becker and Mark Rhodes for making the slotted top and monopole antenna.

[1] W. Joines, Y. Zhang, C. Li, and R. Jirtle, Med. Phys. **21**, 547 (1999).
[2] A. G. Bell, Am. J. Sci. **20**, 305 (1880).
[3] T. Bowen, Ultrasonics Symposium, July 1981 (unpublished).
[4] T. Bowen, U.S. Patent No. 4,385,634 (31 May 1983).

Author complimentary copy. Redistribution subject to AIP license or copyright, see http://rsi.aip.org/rsi/copyright.jsp

[5] T. Bowen, IEEE Trans. Sonics Ultrason. **29**, 187 (1982).
[6] T. Bowen, R. L. Nasoni, A. E. Pifer, and G. H. Sembroski, IEEE Trans. Sonics Ultrason. **29**, 195 (1982).
[7] R. L. Nasoni, S. C. Liew, P. G. Halverson, and T. Bowen, IEEE Trans. Ultrason. Ferroelectr. Freq. Control **33**, 107 (1986).
[8] R. L. Nasoni, S. C. Liew, P. G. Halverson, and T. Bowen, IEEE Trans. Ultrason. Ferroelectr. Freq. Control **33**, 111 (1986).
[9] V. G. Andreev, A. A. Karabutov, and A. A. Oraevsky, IEEE Trans. Ultrason. Ferroelectr. Freq. Control **50**, 1383 (2003).
[10] G. Paltauf, J. A. Viator, S. A. Prahl, and S. L. Jacques, J. Acoust. Soc. Am. **112**, 1536 (2002).
[11] K. P. Kostli and P. C. Beard, Appl. Opt. **42**, 1899 (2003).
[12] J. D. Hamilton and M. O'Donnell, IEEE Trans. Ultrason. Ferroelectr. Freq. Control **45**, 216 (1998).
[13] S. J. Norton and T. Vo-Dinh, J. Opt Soc. Am A **20**, 1859 (2003).
[14] J. J. Niederhauser, M. Jaeger, and M. Frenz, Appl. Phys. Lett. **85**, 846 (2004).
[15] G. Paltauf, H. Schmidt-Kloiber, K. P. Kostli, and M. Frenz, Appl. Phys. Lett. **75**, 1048 (1999).
[16] J. J. Niederhauser, D. Frauchinger, H. P. Weber, M. Frenz, Appl. Phys. Lett. **81**, 571 (2002).
[17] G. Paltauf, H. Schmidt-Kloiber, and M. Frenz, J. Acoust. Soc. Am. **104**, 890 (1998).
[18] G. Paltauf and H. Schmidt-Kloiber, J. Appl. Phys. **82**, 1525 (1997).
[19] G. Paltauf and H. Schmidt-Kloiber, J. Appl. Phys. **88**, 1624 (2000).
[20] S. Sethuraman, S. R. Aglyamov, R. W. Smalling, and S. Y. Emelianov, Ultrasound Med. Biol. **34**, 299 (2008).
[21] S. Sethuraman, S. R. Aglyamov, J. H. Amirian, R. W. Smalling, and S. Y. Emelianov, IEEE Trans. Ultrason. Ferroelectr. Freq. Control **54**, 978 (2007).
[22] B. T. Cox and P. C. Beard, IEEE Trans. Ultrason. Ferroelectr. Freq. Control **54**, 394 (2007).
[23] B. T. Cox, S. R. Arridge, K. P. Kostli, and P. C. Beard, Appl. Opt. **45**, 1866 (2006).
[24] H. F. Zhang, K. Maslov, G. Stoica, and L. V. Wang, Nat. Biotechnol. **24**, 848 (2006).
[25] H. F. Zhang, K. Maslov, M. Sivaramakrishnan, G. Stoica, and L. V. Wang, Appl. Phys. Lett. **90**, 053901 (2007).
[26] R. O. Esenaliev, Y. Y. Petrov, O. Hartrumpf, D. J. Deyo, and D. S. Prough, Appl. Opt. **43**, 3401 (2004).
[27] R. O. Esenaliev, I. V. Larina, K. V. Larin, D. J. Deyo, M. Motamedi, and D. S. Prough, Appl. Opt. **41**, 4722 (2002).
[28] Y. Y. Petrov, I. Y. Petrova, I. A. Patrikeev, R. O. Esenaliev, and D. S. Prough, Opt. Lett. **31**, 1827 (2006).
[29] G. Kim, S. W. Huang, K. C. Day, M. O'Donnell, R. R. Agayan, M. A. Day, R. Kopelman, and S. Ashkenazi, J. Biomed. Opt. **12**, 044020 (2007).
[30] A. Agarwal, S. W. Huang, M. Donnell, K. C. Day, M. Day, N. Kotov, and S. Ashkenazi, J. Appl. Phys. **102**, 064701 (2007).
[31] P. C. Li, C. W. Wei, C. K. Liao, C. D. Chen, K. C. Pao, C. R. Wang, Y. N. Wu, and D. B. Shieh, IEEE Trans. Ultrason. Ferroelectr. Freq. Control **54**, 1642 (2007).
[32] C. W. Wei, S. W. Huang, C. R. Wang, and P. C. Li, IEEE Trans. Ultrason. Ferroelectr. Freq. Control **54**, 1131 (2007).
[33] V. P. Zharov, E. I. Galanzha, E. V. Shashkov, N. G. Khlebtsov, and V. V. Tuchin, Opt. Lett. **31**, 3623 (2006).
[34] Z. Yuan, C. Wu, H. Zhao, and H. Jiang, Opt. Lett. **30**, 3054 (2005).
[35] G. Ku and L. V. Wang, Opt. Lett. **30**, 507 (2005).
[36] M. Eghtedari, A. Oraevsky, J. A. Copland, N. A. Kotov, A. Conjusteau, and M. Motamedi, Nano Lett. **7**, 1914 (2007).
[37] M. Xu and L. V. Wang, Rev. Sci. Instrum. **77**, 041101 (2006).
[38] R. A. Kruger, P. Liu, Y. R. Fang, and C. R. Appledorn, Med. Phys. **22**, 1605 (1995).
[39] R. A. Kruger, K. K. Kopecky, A. M. Aisen, D. R. Reinecke, G. A. Kruger, and W. L. Kiser, Jr., Radiology **211**, 275 (1999).
[40] R. A. Kruger, D. R. Reinecke, and G. A. Kruger, Med. Phys. **26**9, 1832 (1999).
[41] R. A. Kruger, K. D. Miller, H. E. Reynolds, W. L. Kiser, Jr., D. R. Reinecke, and G. A. Kruger, Radiology **216**, 279 (2000).
[42] A. Mashal, J. H. Booske, and S. C. Hagness, Phys. Med. Biol. **54**, 641 (2009).
[43] L. Nie, D. Xing, Q. Zhou, D. Yang, and H. Guo, Med. Phys. **35**, 4026 (2008).
[44] D. Feng, Y. Xu, G. Ku, and L. V. Wang, Med. Phys. **28**, 2427 (2001).
[45] F. John, *Partial Differential Equations*, 4th ed. (Springer, New York, 1982).
[46] S. J. Norton, J. Acoust. Soc. Am. **67**, 1266 (1980).
[47] S. J. Norton and M. Linzer, IEEE Trans. Biomed. Eng. **BME–28**, 202 (1981).
[48] D. V. Finch, S. K. Patch, and Rakesh, SIAM J. Math. Anal. **35**, 1213 (2004).
[49] L. A. Kunyansky, Inverse Probl. **23**, 373 (2007).
[50] D. Finch, M. Haltmeier, and Rakesh, SIAM J. Appl. Math. **68**, 392 (2007).
[51] V. P. Palamodov, J. Fourier Anal. Appl. **6**, 25 (2000).
[52] X. Pan, Y. Zou, and M. Anastasio, IEEE Trans. Image Process. **12**, 784 (2003).
[53] M. Anastasio, J. Zhang, X. Pan, Y. Zou, G. Ku, and L. V. Wang, IEEE Trans. Med. Imaging **24**, 199 (2005).
[54] J. Zhang, M. Anastasio, X. Pan, and L. V. Wang, IEEE Trans. Med. Imaging **24**, 817 (2005).
[55] Y. Xu, L. V. Wang, G. Ambartsoumian, and P. Kuchment, Med. Phys. **31**, 724 (2004).
[56] L. Kunyansky, Inverse Probl. **24**, 055021 (2008).
[57] P. N. T. Wells, *Biomedical Ultrasonics* (Academic, New York, 1977).
[58] F. A. Duck, *Physical Properties of Tissue* (Academic, London, 1990).
[59] A. J. Surowiec, S. S. Stuchly, J. R. Barr, and A. Swarup, IEEE Trans. Biomed. Eng. **35**, 257 (1988).
[60] M. R. Stoneman, M. Kosempa, W. D. Gregory, C. W. Gregory, J. J. Marx, W. Mikkelson, J. Tjoe, and V. Raicu, Phys. Med. Biol. **52**, 6589 (2007).
[61] M. Lazebnik, L. McCartney, D. Popovic, C. B. Watkins, M. J. Lindstrom, J. Harter, S. Sewall, A. Magliocco, J. H. Booske, M. Okoniewski, and S. C. Hagness, Phys. Med. Biol. **52**, 2637 (2007).
[62] M. Lazebnik, D. Popovic, L. McCartney, C. B. Watkins, M. J. Lindstrom, J. Harter, S. Sewall, T. Ogilvie, A. Magliocco, T. M. Breslin, W. Temple, D. Mew, J. H. Booske, M. Okoniewski, and S. C. Hagness, Phys. Med. Biol. **52**, 6093 (2007).
[63] Y. Xu and L. V. Wang, IEEE Trans. Ultrason. Ferroelectr. Freq. Control **53**, 542 (2006).
[64] M. Pramanik, G. Ku, C. Li, and L. V. Wang, Med. Phys. **35**, 2218 (2008).
[65] C. M. Collins, W. Liu, B. J. Swift, and M. B. Smith, Magn. Reson. Med. **54**, 1327 (2005).
[66] P. Berger, D. Pouhe, G. Monich, H. Fahling, P. Wust, and K Peterman, Electron. Lett. **35**, 1317 (1999).
[67] T. Moreno, *Microwave Transmission Line Design Data* (Artech House, Norwood, 1989).
[68] R. Collin, *Field Theory of Guided Waves* (McGraw-Hill, New York, 1960).

Author complimentary copy. Redistribution subject to AIP license or copyright, see http://rsi.aip.org/rsi/copyright.jsp